

Article

Vertical-Longitudinal Coupling Effect Investigation and System Optimization for a Suspension-In-Wheel-Motor System in Electric Vehicle Applications

Ze Zhao ¹, Lei Zhang ^{1,*} , Jianyang Wu ², Liang Gu ¹ and Shaohua Li ³

¹ National Engineering Research Center for Electric Vehicles, Beijing Institute of Technology, Beijing 100081, China

² Beijing Institute of Space Launch Technology, Beijing 100076, China

³ State Key Laboratory of Mechanical Behavior and System Safety of Traffic Engineering Structures, Shijiazhuang Tiedao University, Shijiazhuang 050043, China

* Correspondence: lei_zhang@bit.edu.cn

Abstract: In-wheel-motor-drive electric vehicles have attracted enormous attention due to its potentials of improving vehicle performance and safety. Road surface roughness results in forced vibration of in-wheel-motor (IWM) and thus aggravates the unbalanced electric magnetic force (UEMF) between its rotor and stator. This can further compromise vertical and longitudinal vehicle dynamics. This paper presents a comprehensive study to reveal the coupled vertical–longitudinal effect on suspension-in-wheel-motor systems (SIWMS) along with a viable optimization procedure to improve ride comfort and handling performance. First, a UEMF model is established to analyze the mechanical–electrical–magnetic coupling relationship inside an IWM. Then a road–tire–ring force (RTR) model that can capture the transient tire–road contact patch and tire belt deformation is established to accurately describe the road–tire and tire–rotor forces. The UEMF and the RTRF model are incorporated into the quarter-SIWMS model to investigate the coupled vertical–longitudinal vehicle dynamics. Through simulation studies, a comprehensive evaluation system is put forward to quantitatively assess the effects during braking maneuvers under various road conditions. The key parameters of the SIWMS are optimized via a multi-optimization method to reduce the adverse impact of UEMF. Finally, the multi-optimization method is validated in a virtual prototype which contains a high-fidelity multi-body model. The results show that the longitudinal acceleration fluctuation rate and the slip ratio signal-to-noise ratio are reduced by 5.07% and 6.13%, respectively, while the UEMF in the vertical and longitudinal directions varies from 22.2% to 34.7%, respectively, and is reduced after optimization. Thus, the negative coupling effects of UEMF are minimized while improving the ride comfort and handling performance.

Keywords: in-wheel-motor; unbalanced electric magnetic force; vertical–longitudinal dynamics; road–tire–rotor force; multi-optimization method; virtual prototype



check for updates

Citation: Zhao, Z.; Zhang, L.; Wu, J.; Gu, L.; Li, S. Vertical-Longitudinal Coupling Effect Investigation and System Optimization for a Suspension-In-Wheel-Motor System in Electric Vehicle Applications. *Sustainability* **2023**, *15*, 4168. <https://doi.org/10.3390/su15054168>

Academic Editors: Eric Cheng and Junfeng Liu

Received: 20 January 2023

Revised: 12 February 2023

Accepted: 17 February 2023

Published: 25 February 2023



Copyright: © 2023 by the authors. Licensee MDPI, Basel, Switzerland. This article is an open access article distributed under the terms and conditions of the Creative Commons Attribution (CC BY) license (<https://creativecommons.org/licenses/by/4.0/>).

1. Introduction

Automotive electrification is rapidly expanding worldwide to tackle the formidable challenges of greenhouse gas emissions and fossil oil depletion. In-wheel-motor-drive electric vehicles (IWM EVs) employ four in-wheel-motors (IWMs) installed inside each wheel hub to realize direct propulsion [1–3]. This results in better sprung mass packaging flexibility and can potentially enhance vehicle dynamics stability by independently controlling each IWM [4–6]. Switched Reluctance Motor (SRM) is a reasonable choice for IWM due to its high starting torque, wide speed range and high efficiency [1,7]. However, the motor drive and the suspension system are rigidly connected. Under road roughness excitation, an unbalanced electric magnetic force (UEMF) is generated inside the motor

due to the magnetic gap eccentricity [8]. These form a typical closed-loop mechanical–electrical–magnetic coupling system. The eccentricity caused by the mass imbalance of the motor and by external forces significantly contributes to the UEMF, thus further distorting the magnetic gap distribution and aggravating the amplitude of the electromagnetic excitation [9,10].

Numerous studies have been conducted to mitigate the adverse influence of UEMF on vehicle dynamics. These can be generally grouped into the two categories according to vertical and longitudinal dynamics. For the former, the main approach to reducing vertical UEMF is design optimization for either motor or suspension system. The structure of in-wheel motors can be optimized by altering the rotor and stator geometries or the windings to minimize UEMF [11]. In this regard, Wang et al. [12] investigated the influence of the representative parameters of an in-wheel motor on vehicle vertical dynamics. Similarly, Li et al. [13] introduced parallel paths into the windings to reduce the influence of UEMF on the vibration of the motor. However, these approaches fail to take into account road roughness excitation, and merely optimize the electromagnetic characteristics of the motor. Another method to reduce the vertical UEMF is to optimize suspension design in combination of developing enabling control algorithms. The novel dynamic vibration absorbing structure (DVAS) exemplifies the effort [14], which is installed between the motor and the suspension system to absorb the motor-caused vibration. Previous studies have shown that DVAS can effectively suppress the motor-caused vibration when the spring dampers are properly parameterized [15,16]. However, the proposed integration structure is limited by its complexity, and its efficacy has not been fully validated. On the other hand, various suspension control algorithms have been developed to negate the vertical vibration induced by UEMF. This considers the suspension and in-wheel motor as a complete system and uses active suspension control algorithms to reduce the adverse impact of the increased unsprung mass. The common algorithms include fuzzy logic control [17], ceiling damping control [18], optimal sliding mode control [19], H_∞ control [20], and the like. Nevertheless, the existing studies have invariably neglected the impact of the electromagnetic field, which means that the mechanical–electrical–magnetic coupling effect cannot be fully accounted for.

Axle bows, bearing tolerance and longitudinal velocity variation can lead to the longitudinal eccentricity of the IWM, and the resulting UEMF would further cause the longitudinal vibration [21]. Longitudinal vibration that interacts with the complex elastic structures such as tire may significantly compromise the vehicle traction/braking control performance [22,23]. The UEMF-induced longitudinal vibration can be suppressed via structure optimization and traction/braking force control. For instance, Kambe et al. [24] employed a shock absorber to reduce longitudinal vibration. Similarly, Zuo et al. [25] adopted a flexible connection between the rim and the in-wheel motor to modify the inherent characteristics of electric wheels, resulting in decreased longitudinal vibration. Traction or braking forces can be adjusted through sliding mode control [26], H_2/H_∞ control [27], and direct yaw control [28] in order to mitigate the longitudinal vibration. The existing studies on longitudinal vibration mitigation mainly concentrate on regulating torque ripples, and rarely consider the impact of UEMF. In addition, there is lack of a comprehensive evaluation system that can precisely characterize the longitudinal vibration.

However, the vertical and longitudinal vehicle dynamics are always coupled with each other [29,30]. Several studies have been conducted to reveal the vertical–longitudinal coupling effects for IWMD EVs. For instance, Qin et al. [31] formulated a longitudinal–vertical quarter-vehicle model and analyzed the impact of a random and constant UEMF on vertical and longitudinal vehicle motions. However, this study mainly focused on the influence of the vertical UEMF on longitudinal vehicle motion by assuming a constant longitudinal eccentricity. Chao et al. [32] built a quarter-vehicle longitudinal–vertical coupling model to improve the comprehensive performance of the electro-mechanical braking system. In their study, the evaluation metrics were mainly related to energy efficiency and longitudinal characteristics, neglecting the vertical performance. Ricciardi et al. [33] presented an integrated dynamic control for wheel torque distribution in the longitudinal

direction and for vehicle suspension force in the vertical direction. Their simulation results indicated that this so-called “ride-blending” control can reduce the pitch response of the vehicle body while keeping the dynamic tire force within the safety constraints. However, this study ignored the electro-mechanical coupling effect of IWM, and did not consider the effect of UEMF on vehicle dynamics. Thereby, there is a need to investigate the coupling mechanism of vertical and longitudinal vehicle dynamics caused by UEMF, and their relevant alleviation methods.

Generally, simplified tire models only including spring characteristics are used in vehicle control; however, the increase in unsprung mass and the high-frequency excitation generated by the motor directly affect the working conditions of tires [34]. Typical tire models include physical and empirical models. The brush and ring models are the two main forms of physical models, while the well-known magic formula can be considered as an empirical model. In the existing studies, the Brush and Magic Formula tire models have been used to simulate the tangential tire force characteristics [35,36]. The ring model (RRM) and the flexible ring model (FRM) are commonly used to describe vertical tire dynamics [37,38]. In the RRM, the residual stiffness is introduced between the contact patch and the rigid ring to represent the static tire stiffness in the vertical direction. However, as the tire belt deformation is not considered, this model is only suitable in the lower-frequency ranges [37]. Meanwhile, the FRM employs a large number of segments interconnected by springs and dampers. Its bandwidth is beyond the frequency range of 150 Hz; however, it can occasionally describe the low-frequency characteristics [38]. As for IWMD EVs, its vertical motion is exposed to both high- and low-frequency excitations [22]. Consequently, in order to comprehensively analyze the vertical–longitudinal coupling characteristics of the road–tire–IWM system, it is necessary to integrate the above-mentioned tire models for better representation.

As described above, there are two obvious vertical–longitudinal coupling systems existing in IWMD EVs. These are the electromechanical–magnetic coupling system and the road–tire–IWM system; the UEMF and the road–tire–rotor force (RTRF) are their respective characteristic forces. Therefore, it is necessary to build an accurate and comprehensive model to investigate the influence of these two systems on vehicle vertical–longitudinal dynamics. The exclusive contributions of this study are summarized as follows.

1. A UEMF model is established and used as an internal excitation of the suspension-in-wheel-motor system (SIWMS). The electro-mechanical mechanism of UEMF and its effect on vehicle vertical–longitudinal dynamics are comprehensively studied under various road conditions.
2. A RTRF model that can capture the transient tire–road contact patch and tire belt deformation is proposed to accurately describe the vertical–longitudinal coupling effect of the road–tire–motor system. The RTRF model is then incorporated into the SIWMS model for better modelling accuracy.
3. A comprehensive evaluation system is proposed to describe the vertical–longitudinal dynamics of IWMD EVs. The ride comfort and handling performance are improved by optimizing the key parameters of the SIWMS.

The remainder of this paper is organized as follows. Section 2 introduces the quarter-SIWMS model by incorporating the UEMF and the RTRF model. Section 3 provides the verification of the SIWMS model in a virtual prototype by establishing a high-fidelity multi-body vehicle model. Section 4 elaborates on the UEMF effects on the coupled vertical and longitudinal vehicle motions and presents the details on parameters optimization of the SIWMS. Finally, our key conclusions are summarized in Section 5.

2. The Quarter-SIWMS Model

The primary objective of this study is to fully understand the electro-mechanical-magnetic coupling effects of IWMD EVs. Hence, a precise vehicle dynamics model is established to reveal the contributions of different factors. In this study, the quarter-SIWMS

model consists of three sub-models: (1) the excitation source model, (2) the RTRF model, and (3) the nonlinear three-directional coupled (NTDC) model.

2.1. The Excitation Source Model

The SIWMS model is characterized by the internal and the external excitation. The internal excitation is the investigated UEMF, while the external excitation is mainly ascribed to the road roughness.

2.1.1. The UEMF Model

In this study, a 5-kW exterior rotor SRM with 8/6-four phases [39] is selected as the IWM IWMD EVs. For an SRM, the radial and tangential components of the electromagnetic force depend on the radial and tangential components of the flux density [40]. As the magnetic permeability of the air gap is much lower than that of the ferromagnetic material, the radial component of the flux density is greater than the tangential [41,42]. This is verified by existing studies, which have shown that the radial force is about 16.6 times more than the tangential force in an SRM [43]. This means the rotor and stator eccentricity can cause a large radial force, leading to severe vibration issue. The UEMF is produced by the coupled effects of the electromagnetic and mechanical fields, and represents the resultant global magnetic force acting on the rotor and stator due to the asymmetric magnetic field distribution in the air gap. The UEMF generation process is shown in Figure 1, where F_e is the electromagnetic force, F_t is the tangential force and F_r is the radial force.

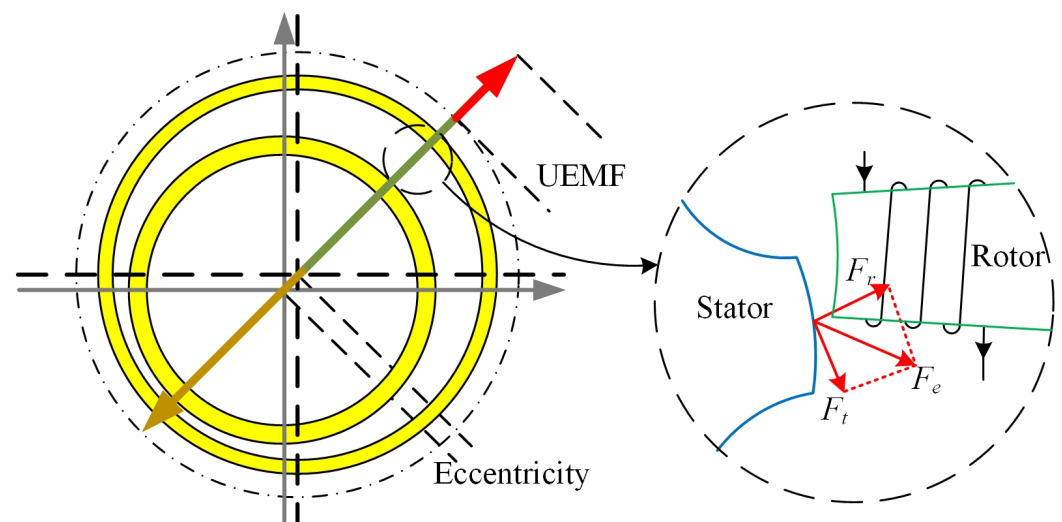


Figure 1. The generated UEMF in an SRM.

For SRMs, the magnetic co-energy $W(i, \theta)$ is determined according to the current i and the phase inductance $L(\theta, i)$, where θ is the rotor angle. The first three terms of the Fourier expansion are given by

$$L(\theta, i) = L_0(i) + L_1(i) \cos(N_r\theta + \pi) + L_2(i) \cos(2N_r\theta + 2\pi) \quad (1)$$

where L_0 , L_1 , and L_2 are calculated by

$$\begin{cases} L_0(i) = \frac{1}{2} \left[\frac{1}{2}(L_a(i) + L_u) + L_m(i) \right] \\ L_1(i) = \frac{1}{2} (L_a(i) - L_u) \\ L_2(i) = \frac{1}{2} \left[\frac{1}{2}(L_a(i) + L_u) - L_m(i) \right] \end{cases} \quad (2)$$

where L_a , L_u , and L_m are the inductances at the fully aligned ($\theta = 30^\circ$), unaligned ($\theta = 0^\circ$), and intermediate positions, respectively. These parameters can be fitted with polynomials

based on finite element or experimental analysis. Considering the relationship between the flux and the inductance, the k -th phase flux linkage can be derived as

$$\begin{aligned}\psi(\theta, i_k) &= \int_0^{i_k} L(i_k, \theta) di_k \\ &= \frac{1}{2} [\cos^2(N_r \theta) - \cos(N_r \theta)] \sum_{n=0}^N c_n i^n \\ &\quad + \sin^2(N_r \theta) \sum_{n=0}^N d_n i^n \\ &\quad + \frac{1}{2} L_u i_k [\cos^2(N_r \theta) + \cos(N_r \theta)]\end{aligned}\quad (3)$$

where ψ is the flux linkage, N_r is the number of salient poles in the rotor, $c_n = a_n - 1/n$ and $d_n = b_n - 1/n$. According to the Faraday's law, the phase voltage can be derived by

$$U_k = R_k i_k + \frac{d\psi_k}{dt} = R_k i_k + L_k(\theta, i_k) \frac{di_k}{dt} + \omega \frac{\partial \psi_k}{\partial \theta} \quad (4)$$

where ω is the rotational speed of the rotor. The phase current can be given by

$$i_k = \int \frac{U_k - R_k i_k - \omega \frac{\partial \psi_k}{\partial \theta}}{L_k(\theta, i_k)} dt \quad (5)$$

For the constant phase current i , the relationships between the magnetic co-energy $W(i, \theta)$, torque T , and radial force F_r can be obtained by

$$T = \left. \frac{\partial W(\theta, i)}{\partial \theta} \right|_{i=\text{const}}, F_r = \left. \frac{\partial W(\theta, i)}{\partial l_g} \right|_{i=\text{const}} \quad (6)$$

where l_g is the air gap between the rotor and the stator. The phase torque can be deduced by

$$\begin{aligned}T_k &= \left. \frac{\partial W(\theta, i)}{\partial \theta} \right|_{i=\text{const}} = \int_0^{i_k} \frac{\partial \psi(\theta, i_k)}{\partial \theta} di_k \\ &= \sin(N_r \theta) \sum_{n=1}^N \frac{1}{n} e_{n-1} i_k^n + \sin(2N_r \theta) \sum_{n=1}^N \frac{1}{n} f_{n-1} i_k^n\end{aligned}\quad (7)$$

where both e and f are the intermediate functions. The former, e , can be obtained by $e_n = (1/2)N_r c_n$ with $e_1 = (1/2)N_r(c_1 - L_u)$. The latter, f , can be calculated by $f_n = N_r d_n - e_n$ with $f_0 = 0$ and $f_1 = (1/2)N_r(2d_1 - c_1 - L_u)$.

Based on the phase torque T_k , the radial force of the k th phase can be calculated by [44]

$$F_{rk} = -\frac{T_k \delta}{l_g} \quad (8)$$

where δ is the overlap between the rotor and the stator. The presence of the non-zero l_g , known as eccentricity, results in UEMF. The UEMF is defined as a difference in the radial forces between the two opposing stator poles. There are many reasons for eccentricity, such as poor manufacturing accuracy or dynamic coupling effects [45]. The air gap eccentricity l_g can be decomposed into two resultant components denoted as ε_x and ε_z . In this study, the air gap in the x -direction that is caused by axle bows, bearing tolerance and longitudinal road inputs is denoted as ε_x . The dynamic eccentricity in the z -direction, defined as ε_z , describes the dynamic coupling effect of the suspension, IWM, and road roughness. The relationship between the UEMF, its components (i.e., F_{uv} and F_{ul}), and mixed eccentricity is depicted in Figure 2.

Based on the definitions of UEMF and mixed eccentricity, the vertical UEMF F_{uv} can be calculated as [14]

$$F_{uv} = \sum_{k=1}^4 \left[\left(-\frac{T_k \delta}{l_g - \varepsilon_y \cos \beta_k} + \frac{T_k \delta}{l_g + \varepsilon_y \cos \beta_k} \right) \cos \beta_k \right] \quad (9)$$

Similarly, the longitudinal UEMF F_{ul} is provided by

$$F_{ul} = \sum_{k=1}^4 \left[\left(\frac{T_k \delta}{l_g - \varepsilon_x \sin \beta_k} - \frac{T_k \delta}{l_g + \varepsilon_x \sin \beta_k} \right) \sin \beta_k \right] \quad (10)$$

where β is the phase structure angle ($\beta_1 = 0^\circ, \beta_2 = 45^\circ, \beta_3 = 90^\circ$ and $\beta_4 = 135^\circ$) and the nominal air gap is 0.8 mm.

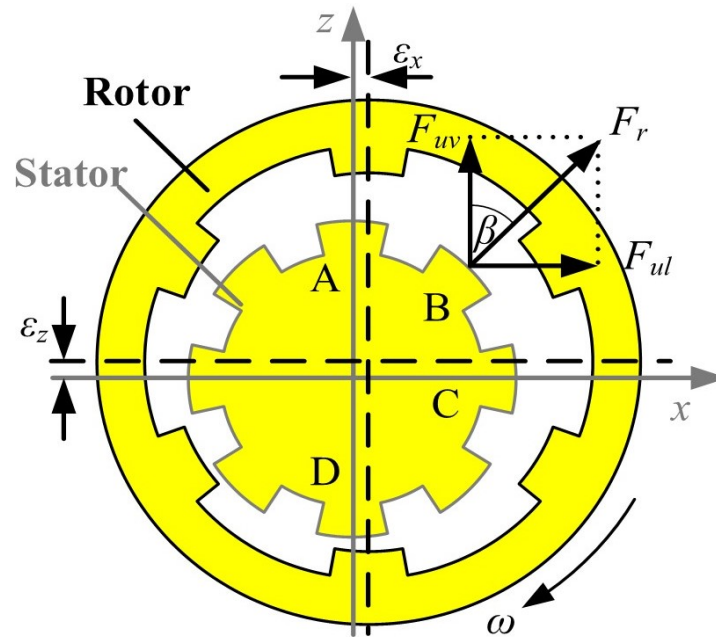


Figure 2. The vertical and longitudinal UEMFs induced by eccentricity.

Current chopping control is utilized to get a steady operation of SRM. According to the configuration of the adopted SRM model, θ_{on} and θ_{off} are selected as 28° and 60° , respectively [31]. Based on Equations (9) and (10), it can be deduced that the single-phase UEMFs of SRM in both vertical and longitudinal directions are characterized by different ε_x and ε_z values for $\theta_{on} = 28^\circ$ and $\theta_{off} = 60^\circ$. The results are shown in Figure 3. It can be seen that the eccentricity can directly affect UEMF, which is represented in the form of the electromagnetic coupling. To ensure an efficient and stable braking process, the UEMF should be explored as the main internal excitation.

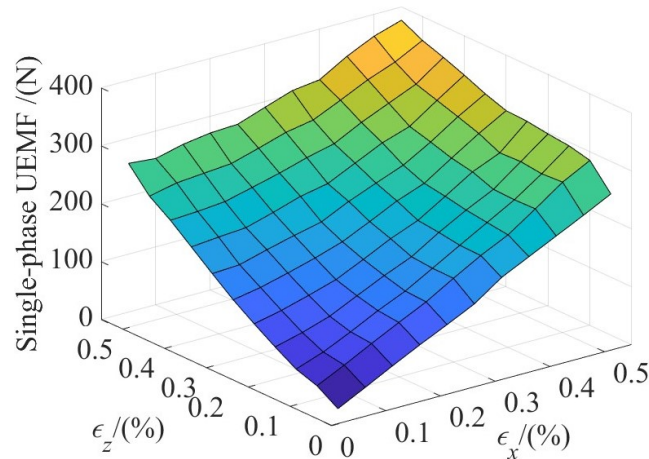


Figure 3. The influence of eccentricities on UEMF.

2.1.2. Road Inputs Model

The road inputs model contains road grade (*RG*) and road type (*RT*). *RG* acts on the vehicle as vertical road profiles, while *RT* characterizes the longitudinal road friction.

(1) Vertical road input

The statistical characteristics of *RG* are commonly described by the power spectral density in the vertical direction. The harmonic superposition algorithm is used to generate time-domain road profiles as [46,47]

$$q(t) = \sum_{K=1}^M \sqrt{2 \cdot G_q(f_{\text{mid}-K}) \cdot \frac{f_2 - f_1}{M}} \sin(2\pi f_{\text{mid}-K}t + \phi_K) \quad (11)$$

where $q(t)$ is the generated road profile, $f_{\text{mid}-K}$ is the K -th middle frequency, $G_q(f_{\text{mid}-K})$ is the power spectral density at $f_{\text{mid}-K}$, ϕ_K is an identifiably distributed phase with the range of $(0, 2\pi)$, and the upper and lower time-domain frequency boundaries are denoted as f_1 and f_2 .

As vehicle speed is variable during braking, the independent variable needs to be changed from time to braking distance by

$$q(t) = q(\text{dis})|_{\text{dis}=v_c \cdot t} \quad (12)$$

where v_c is the conversion speed and dis is the braking distance at time t .

(2) Longitudinal road input

One major parameter used for the longitudinal road input is the road–tire adhesion coefficient $\mu(\lambda)$, which can be expressed as

$$\mu(\lambda) = c_1 \left(1 - e^{-c_2 \lambda}\right) - c_3 \lambda \quad (13)$$

where c_1 , c_2 , and c_3 define the road friction conditions (see Table 1) [48] and λ is the tire slip ratio. The optimal slip ratio λ^* for different road conditions is located in the far right-hand column of Table 1.

Table 1. Parameters of different road surfaces.

Road Type	c_1	c_2	c_3	λ^*
Dry asphalt	1.28	23.99	0.52	0.17
Dry cement	1.20	25.17	0.54	0.16
Wet asphalt	0.86	33.82	0.35	0.13
Cobblestone	0.40	33.71	0.12	0.14
Snow	1.20	94.13	0.06	0.06
Ice	0.05	306.39	0	0.03

2.2. RTRF Model

The IWM–tire system consists of a rigid rotor and a deformable tire belt that are connected by springs and dampers in the radial and torsional directions, respectively [49]. By separately capturing the transient road–tire contact patch and tire belt deformation, the RTRF model can accurately reveal the road–tire and tire–rotor forces [50,51]. The RTRF model can be divided into two main parts, i.e., the contact force in the contact patch and the deformation force between the tire belt and the rotor.

2.2.1. Road–Tire Force

(1) Vertical contact force

When a tire is loaded on the road, a large deformation may occur near the contact patch, and a limited contact length that can be simplified to a contact point [50]. Vertical residual stiffness is introduced to obtain the overall vertical tire stiffness [52].

The vertical force at the contact point F_{cZ} is directly related to the vertical residual stiffness k_{rs} . By neglecting higher-order terms, a third-order polynomial is used to describe the vertical force due to the residual tire deflection [37], which is given by

$$F_{cZ} = q_{Fzr3}k_{rs}^3 + q_{Fzr2}k_{rs}^2 + q_{Fzr1}k_{rs} \quad (14)$$

where ω_t is the rotational speed of tire and q_{Fzr*} represents the polynomial coefficients, which can be given by

$$\begin{cases} q_{Fzr1} = k_{trd} \frac{q_{Fz1}(1+q_{V2}|\omega_t|)}{k_{trd}-q_{Fz1}(1+q_{V2}|\omega_t|)} \\ q_{Fzr2} = k_{trd} \frac{k_{trd}(k_{trd} \cdot q_{Fz2} + q_{Fzr1} \cdot q_{Fz2})(1+q_{V2}|\omega_t|)}{(k_{trd}-q_{Fz1}(1+q_{V2}|\omega_t|))^2} \\ q_{Fzr3} = 2k_{trd} \frac{q_{Fz2} \cdot q_{Fz2}(1+q_{V2}|\omega_t|)}{(k_{trd}-q_{Fz1}(1+q_{V2}|\omega_t|))^2} \end{cases} \quad (15)$$

where q_{V1} and q_{V2} are the vertical stiffness correlation coefficients of the tire and k_{trd} is the tire sidewall stiffness.

Then, the residual stiffness is derived as

$$k_{rs} = q(dis_{cp}) - z_t + q_{V1}\omega_t^2 \quad (16)$$

where dis_{cp} , z_t , and $q(dis_{cp})$ are the braking distance, vertical displacement, and effective road roughness at the contact point, respectively.

(2) Longitudinal contact force

For the longitudinal tire model, as the deformation of the sidewall is already represented by the displacement of the tire belt, only a slip model for the contact patch is required. The elastic deformation of the tire sidewall results in a difference between the rotor's and the tire's linear velocity in the contact patch [53,54]. The delay of the contact patch's response to a change in slip (the relaxation length of the contact patch) is approximated with a first-order filter, which is given by [55]

$$\sigma_c \dot{\lambda}_d + |\nu_{cr}| \lambda_d = -\nu_{c,sx} \quad (17)$$

where λ_d is the tire slip ratio calculated by the first-order filter, σ_c is the relaxation length of the contact patch, and ν_{cr} is the linear velocity at the contact patch. The parameter $\nu_{c,sx}$ is the slip velocity at the contact patch, while ν_{cr} and $\nu_{c,sx}$ are expressed as

$$\nu_{cr} = r_e \omega_t, \nu_{c,sx} = \nu_t - r_e \omega_t \quad (18)$$

where r_e is the effective rolling radius and ν_t is the forward velocity of the wheel center. The slip velocity of an elastic tire can be defined as the absolute speed of an imaginary point. The effective rolling radius r_e is defined such that the slip velocity is zero for free rolling. The effective rolling radius can be expressed in the form of a third-order polynomial, which is given by

$$r_e = q_{re3} \sqrt{F_{cZ}^3} + q_{re2} \sqrt{F_{cZ}^2} + q_{re1} \sqrt{F_{cZ}} + q_{re0} + q_{V1} \omega_t^2 \quad (19)$$

where q_{re0} , q_{re1} , q_{re2} , and q_{re3} are the rolling correlation coefficients.

Under full adhesion, σ_c is equal to half of the contact length [56], which is given by

$$\begin{cases} F_Z = (m_s + m_{ms} + m_{mr} + m_t)g - F_{cZ} \\ \sigma_c = \frac{q_{a2} \sqrt{F_Z^2} + q_{a1} \sqrt{F_Z}}{2} \end{cases} \quad (20)$$

where F_Z is the normal force, m_s is the quarter sprung mass of the vehicle, m_{mr} is the mass of the motor, m_{ms} is the stator and axle mass, m_t is the mass of the tire, and q_{a1} and q_{a2} represent the contact length correlation coefficients. According to Equations (19) and (20), the vertical forces F_{cZ} and F_Z play decisive roles in determining the vertical-longitudinal road-tire coupling effect.

A friction model is used to describe the longitudinal forces at the contact patch as a function of the slip ratio. The empirical magic formula is adopted, which is provided by [36]

$$F_{cX} = F_Z \mu(\lambda_d) \sin(C \arctan(B \lambda_d - E(B \lambda_d - \arctan(B \lambda_d)))) \quad (21)$$

where F_{cX} is the longitudinal friction force, B , C , and E are the model parameters. It can be observed that the slip ratio has an enormous influence on the longitudinal tire force and that the longitudinal and vertical motions are highly coupled.

In practice, the slip ratio is defined according to the difference between the longitudinal velocity of the vehicle and the linear velocity of the wheel, which can be obtained by

$$\lambda_c = \frac{v_{ms} - \omega_{mr} R_t}{v_{ms}} \quad (22)$$

where λ_c is the measured slip ratio, v_{ms} is the longitudinal vehicle velocity, and ω_{mr} is the rotational speed of the rotor. It is worth noting that the changes in the effective rolling radius and tire contact patch are ignored, as these would introduce significant errors into the dynamic process. The relative error of the slip ratio estimation is defined as

$$e_{slip}(t) = \lambda_d(t) - \lambda_c(t) \quad (23)$$

where e_{slip} is the error between the slip ratios from the established and the conventional model, which is used as an important indicator for vehicle dynamics performance in the later analysis.

2.2.2. Tire–Rotor Force

Although $q(dis)$ is taken as the vertical input from road profiles, it may induce tire deformation in both the vertical and longitudinal directions. The tire force model can be described by a finite number of independent radial spring and damping elements evenly distributed in the lower semicircle, as shown in Figure 4 [56]. The total number of the discrete radial elements is denoted by N_{tr} [57]. In Figure 4, z_{mrc} is the vertical coordinate at the center of the rotor, z_t is the vertical displacement of the contact point, and α_i represents the angle between an arbitrarily chosen element and the vertical that ranges from $-\arcsin(\sigma_c/R_t)$ to $+\arcsin(\sigma_c/R_t)$. For the positive x -axis, the subscript i indicates the sequence number of the element that ranges from 1 to N_{tr} , while $\gamma_{\alpha i}$, $dis_{\alpha i}$, and $q(dis_{\alpha i})$ are the radial deformation, braking distance, and road elevation of the element, respectively. As a result of tire deformation, the vertical component $F_{tz\alpha i}$ and longitudinal component $F_{tx\alpha i}$ of the radial spring and damping element forces are provided by

$$\begin{cases} F_{tz\alpha i} = \begin{cases} (\gamma_{\alpha i} k_{trd} + \dot{\gamma}_{\alpha i} c_{trd}) \cos \alpha i & \gamma_{\alpha i} > 0 \\ \dot{\gamma}_{\alpha i} c_{trd} \cos \alpha i & \gamma_{\alpha i} \leq 0 \end{cases} \\ F_{tx\alpha i} = \begin{cases} (\gamma_{\alpha i} k_{trd} + \dot{\gamma}_{\alpha i} c_{trd}) \sin \alpha i & \gamma_{\alpha i} > 0 \\ \dot{\gamma}_{\alpha i} c_{trd} \sin \alpha i & \gamma_{\alpha i} \leq 0 \end{cases} \end{cases} \quad (24)$$

where c_{trd} is the tire sidewall translational damping. The deformation and deformation rate of a certain radial element can be approximately calculated by

$$\begin{cases} \alpha i = -\arcsin(\sigma_c/R_t) + 2i \arcsin(\sigma_c/R_t)/N_{tr} \\ dis_{\alpha i} = x_t + \sqrt{(R_t^2 - \sigma_c^2)} \cdot \tan \alpha i \\ (R_t - \gamma_{\alpha i}) \cos \alpha i + q(dis_{\alpha i}) = R_t + z_{mrc} + z_t \end{cases} \quad (25)$$

where x_t is the longitudinal displacement of the tire. The vertical component F_{tz} and longitudinal component F_{tx} of the tire–rotor force caused by tire deformation at the rotor's center can be obtained by summing the force components of each spring and damping element. These can be obtained by

$$\begin{cases} F_{tz} = \sum_{i=1}^{N_{tr}} F_{txxi} \\ F_{tx} = \sum_{i=1}^{N_{tr}} F_{tz\alpha i} \end{cases} \quad (26)$$

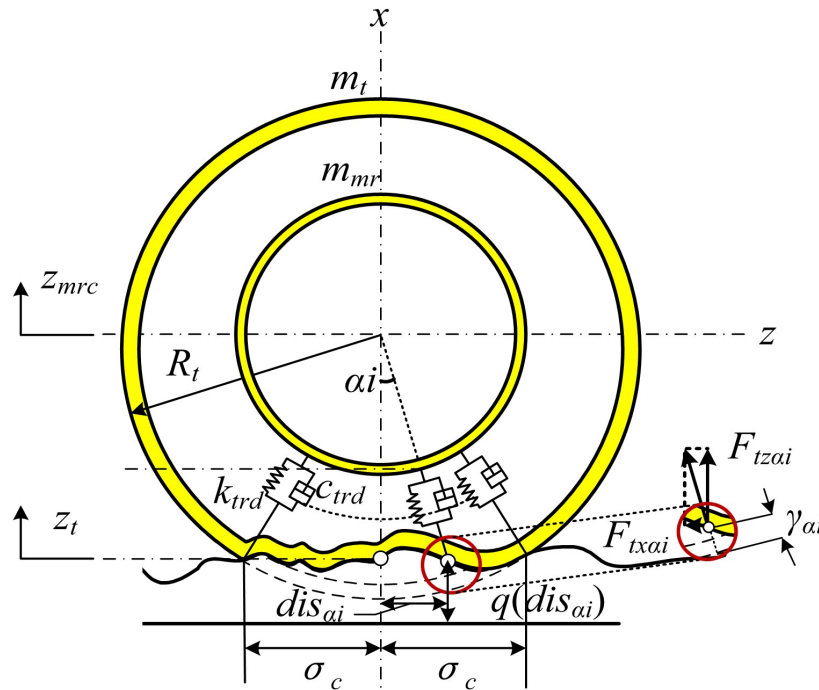


Figure 4. The tire-rotor force.

2.3. NTDC Model

To reveal the vibration mechanism of IWMD EVs under the electromagnetic coupling, the NTDC model describing the vertical, longitudinal, and rotational motions is established as shown in Figure 5. Based on the Newton’s law, the equation of vibration is given by

$$\begin{cases} m_t \ddot{z}_t + F_{tz} + F_{cZ} = 0 \\ m_{mr} \ddot{z}_{mr} - F_{tz} + F_{bv} - F_{uv} = 0 \\ m_{ms} \ddot{z}_{ms} + F_{sus} - F_{bv} + F_{uv} = 0 \\ m_s \ddot{z}_s - F_{sus} = 0 \\ F_{bv} = k_{beaz}(z_{mr} - z_{ms}) \\ F_{sus} = c_{sus}(\dot{z}_{ms} - \dot{z}_s) + k_{trd}(z_{ms} - z_s) \\ q_a m_t \dot{x}_t - F_{cX} + F_{tl} + F_{roll} = 0 \\ m_{mr} \dot{x}_{mr} - F_{tl} - F_{bl} + F_{ul} = 0 \\ m_{ms} \dot{x}_{ms} + F_{bl} - F_{ul} + F_{usl} = 0 \\ m_s \dot{x}_s - F_{usl} + F_{air} = 0 \\ F_{tl} = c_{trd}(\dot{x}_t - \dot{x}_{mr}) + k_{trd}(x_t - x_{mr}) - F_{tx} \\ F_{bl} = k_{bear}(x_{mr} - x_{ms}) \\ F_{usl} = c_{ux}(\dot{x}_{ms} - \dot{x}_s) + k_{ux}(x_{ms} - x_s) \\ F_{roll} = \mu_{roll} \dot{x}_t \\ F_{air} = k_{air} \dot{x}_s^2 \end{cases} \begin{cases} I_t \ddot{\theta}_t + T_t + r_e F_{cX} = 0 \\ I_{mr} \ddot{\theta}_{mr} - T_t - T_b - T_{IWM} = 0 \\ T_t = c_{trt}(\dot{\theta}_t - \dot{\theta}_{mr}) + k_{trt}(\theta_t - \theta_{mr}) \end{cases} \quad (27)$$

where I_t is the tire ring inertia, I_m is the rim and rotor inertia, k_{trt} is the tire sidewall rotational stiffness, c_{trt} is the tire sidewall rotational damping, k_{bear} is the motor bearing stiffness, k_{sus} is the suspension stiffness, c_{sus} is the suspension damping, k_{ux} is the shaft sleeve stiffness, c_{ux} is the shaft sleeve damping, z_i is the vertical displacement of components, F_{bv} and F_{bl} are the vertical and longitudinal motor bearing forces, F_{sus} is the suspension vertical force, x_i is the longitudinal displacement of components, F_{tl} is the

longitudinal tire force, F_{usl} is the longitudinal suspension and shaft sleeve force, F_{air} and F_{roll} are the rolling resistance and air drag, μ_{roll} and k_{air} are the coefficients of F_{air} and F_{roll} , θ_i is the rotational angle, T_t is the internal tire torque, T_{IWM} is the braking torque of the motor, and T_b is the braking torque of the brake caliper.

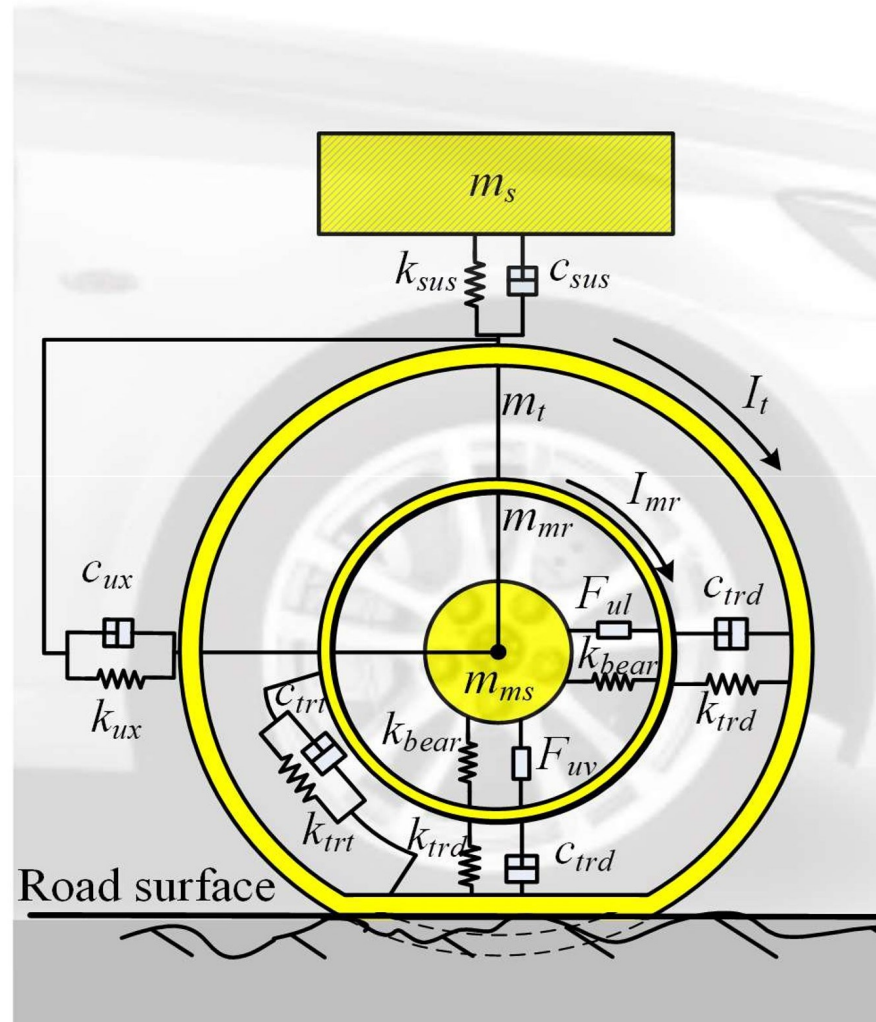


Figure 5. The NTDC vibration coupling model.

The schematic of the vibration model is illustrated in Figure 6. Theoretically, the vertical and longitudinal coupling effect occurs in UEMF during the braking process. As previously mentioned, ε_z in the vertical direction and ε_x in the longitudinal direction represent the eccentricity of motor due to the road surface roughness and braking torque, respectively, while ε_z and ε_x synthesize the radial eccentricities to produce the radial UEMF by decoupling phase structure angle; that is to say, the coupling effect between ε_z and the IWM system produces F_{uv} . The vertical UEMF and eccentricity are characterized by the coupling effect under road inputs. Similar to the vertical process, F_{cx} directly influences ε_x in the longitudinal vibration dynamics, which further produces F_{ul} within its coupling process in the IWM system.

The vertical–longitudinal coupling effect exists in the RTRF model as well. External excitations have two main sources, i.e., RG and RT . For a given road profile, the longitudinal vehicle velocity determines the vertical road input z_r (RG). In the road–tire force model, the vertical load of the tire is a direct determinant of r_e and σ_c . For the tire–rotor force model, the radial deformation forces are decoupled into vertical and longitudinal forces, which serve as the inputs to the vertical and longitudinal vibration dynamics modules. In the

SIWMS model, the vertical–longitudinal coupling effect is significant due to the unique structure of IWM.

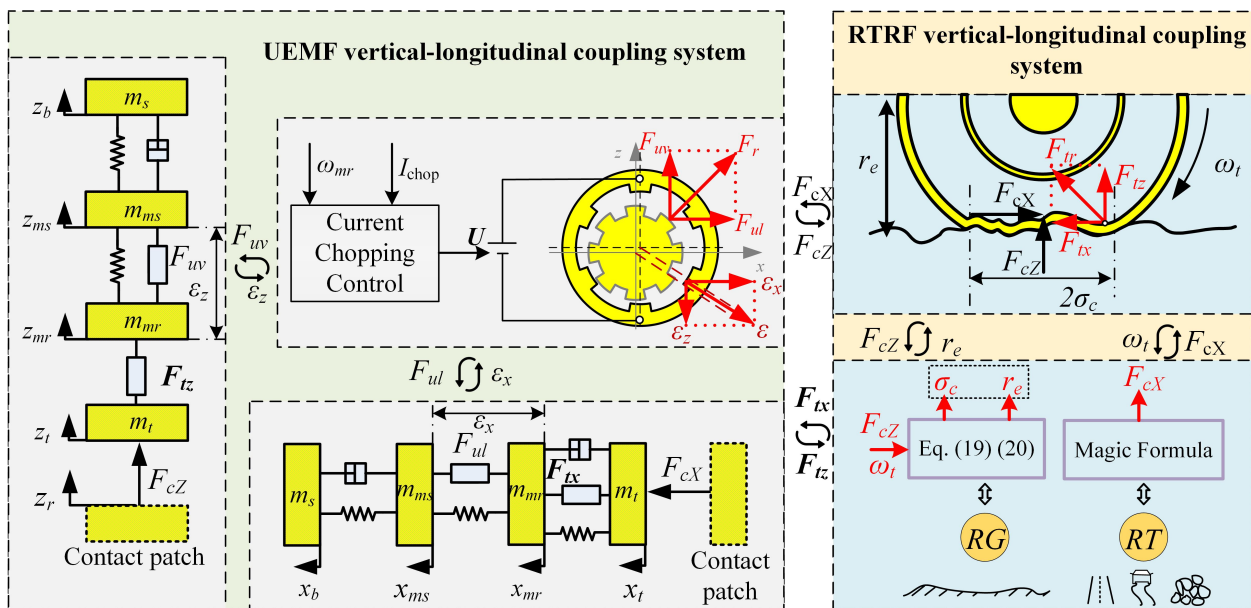


Figure 6. The vertical–longitudinal coupling in the quarter-SIWMS model with the red fonts indicating the coupling variables.

3. Simulation and Verification of the Quarter-SIWMS Model

3.1. SIWMS Simulation Model

According to the established SIWMS model, a simulation platform was developed in the MatLab /Simulink. Braking maneuvers were performed for model verification. The specifications of the test vehicle are listed in Table 2. The tire is a summer tire for passenger cars, which is designated as 205/55R16 [58].

Table 2. The specifications of the test vehicle.

Parameters	Value	Parameters	Value	Parameters	Value
Effective rolling radius		Vertical sidewall stiffness		IWM and vehicle parameters	
R_t	0.3160 m	q_{V1}	$8.5352 \times 10^{-8} \text{ m s}^2$	c_{ux}	1800.39 N·s/m
q_{re0}	0.3164 m	q_{V2}	$8.81 \times 10^4 \text{ s}$	k_{ux}	$2.5 \times 10^4 \text{ N/m}$
q_{re1}	$-9.3972 \times 10^{-4} \text{ m}$	q_{Fz1}	$1.4389 \times 10^5 \text{ N/m}$	k_{sus}	$3.2 \times 10^4 \text{ N/m}$
q_{re2}	$-9.3972 \times 10^{-6} \text{ m}$	q_{Fz2}	$4.5090 \times 10^6 \text{ N/m}^2$	c_{sus}	$1.8 \times 10^3 \text{ N·s/m}^2$
q_{re3}	$-3.0346 \times 10^{-8} \text{ m}$	Tire parameters		k_{bear}	$2.08 \times 10^7 \text{ N/m}$
Contact patch		I_t	0.546 kg·m^2	k_{air}	$5.3 \times 10^{-3} \text{ N/m}$
q_{a1}	$1.478 \times 10^{-3} \text{ m}$	I_{mr}	0.417 kg·m^2	m_{ms}	9.5 kg
q_{a2}	$-5.6829 \times 10^{-6} \text{ m/N}$	m_t	6.15 kg	m_{mr}	22.5 kg
μ_{roll}	0.015 N·s/m			m_s	332 kg
Magic Formula		c_{trd}	510 N·s/m		
B	20.2937	k_{trd}	$1.8 \times 10^6 \text{ N/m}$		
C	1.9655	k_{trt}	$5.1 \times 10^4 \text{ N/m}$		
E	0.8613	c_{trt}	$20 \times \text{N·s/m}$		

For road inputs, four typical conditions were taken as the excitation sources acting on the SIWMS model. They are the ISO-A, ISO-B, dry asphalt, and cobblestone as shown in Figure 7. The road roughness was transformed from time-dependent to braking distance-dependent, as shown in Figure 7a. Sequentially, the modification of each response variable was then obtained under the excitation sources.

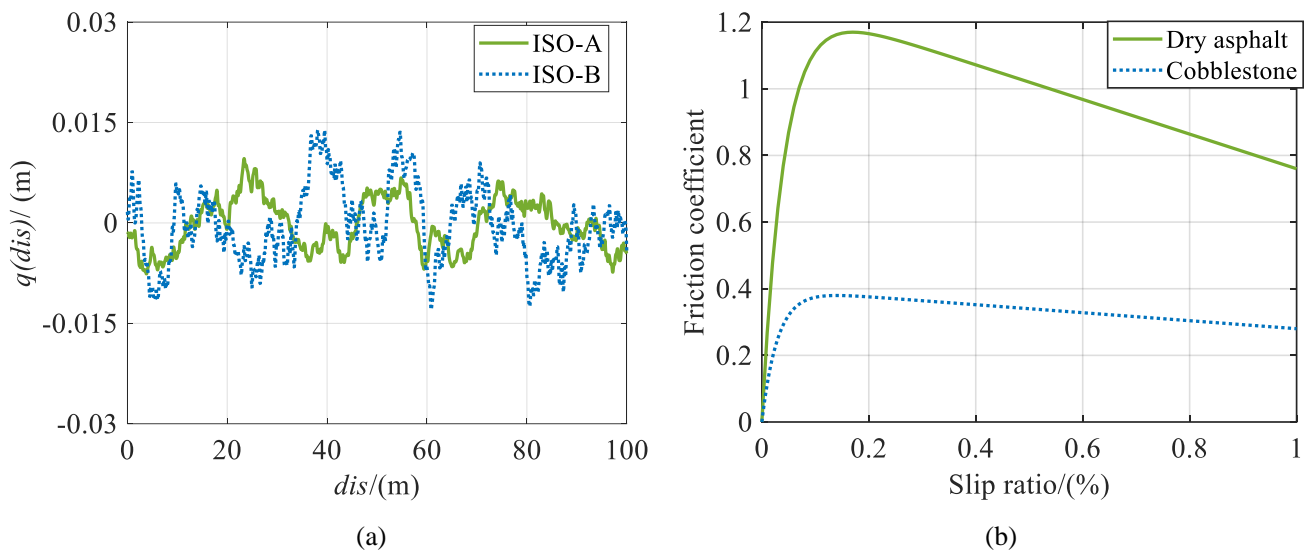


Figure 7. Four typical conditions of road inputs: (a) RG and (b) RT.

3.2. Brake Control System

The braking torque is provided by the hydraulic braking system (HBS). The vehicle control unit (VCU) obtains the rotational speed of IWM and calculates the slip ratio λ_c according to Equation (22). Then, the VCU delivers the difference between the optimal and the actual slip ratio to the ABS module at each time step.

The initial longitudinal vehicle velocity was set to be 60 km/h and the ABS cut-off vehicle velocity was set to be 5 km/h. Before verifying the proposed model, the efficacy of the PID controller for optimal slip ratio tracking needs to be verified. The control performance for a vehicle traveling on the ISO-A, ISO-B, dry asphalt, and cobblestone road conditions while executing braking at 60 km/h is shown in Figure 8. It can be seen that the PID controller is able to closely track the desired slip ratios under different road frictions.

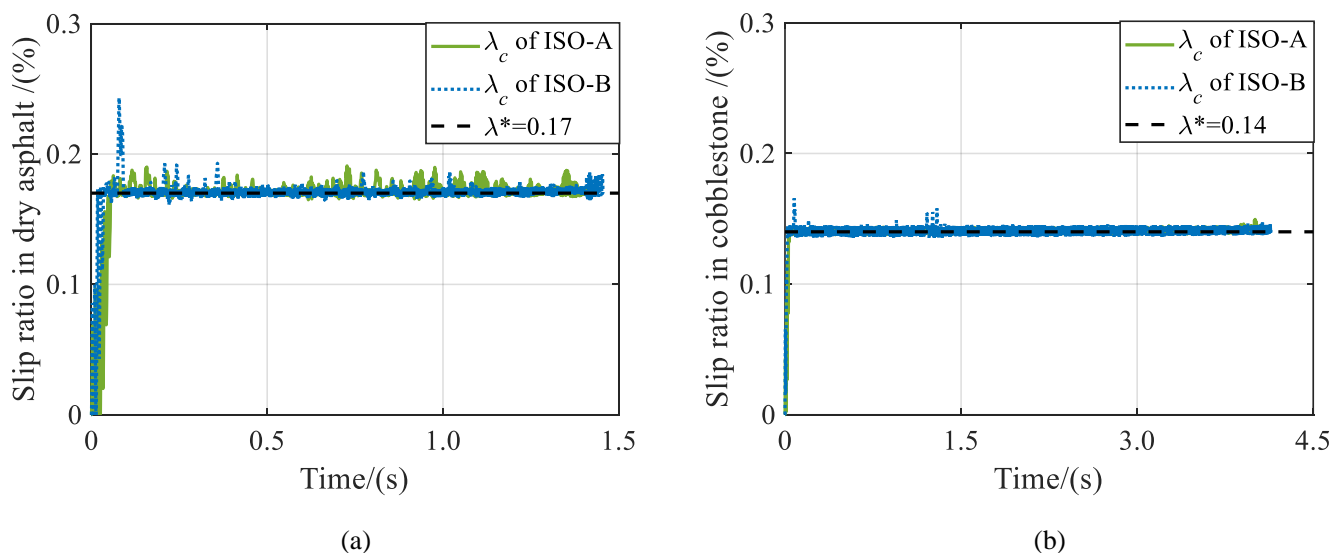


Figure 8. The actual slip ratio on (a) the dry and (b) the cobblestone road during optimal ratio tracking control.

3.3. Vertical–Longitudinal Dynamics Evaluation Indexes

To examine the vertical dynamics during the braking process, the root mean squared (RMS) errors of the vertical acceleration (RVA) and of the tire dynamic load (RTDL) were

selected to represent the vehicle response, which can reflect the ride comfort and handling performance, respectively. The longitudinal vibration is an important indicator of driving performance assessment. Usually, the longitudinal vibration is characterized by the frequency and attitude or power spectrum of the longitudinal vehicle acceleration or jerk (the derivative of acceleration), which happens with greater amplitude in specific transient operating conditions such as rapid acceleration and emergency braking [59]. Therefore, the longitudinal acceleration fluctuation rate (LAFR) was selected, which is provided by

$$\text{LAFR} = \frac{\sqrt{\frac{1}{t} \int_0^t \left[a_x(t) - \frac{1}{t} \int_0^t (a_x(t) dt)^2 \right] dt}}{\frac{1}{t} \int_0^t (a_x(t) dt) dt} \quad (28)$$

where a_x is the instantaneous longitudinal vehicle acceleration and t is the braking time.

The tire slip ratio is a key parameter during braking. For the IWM system, the tire slip ratio fluctuates more dramatically due to the torque fluctuation and UEMF. In addition, the increase of inertia around the axle can aggravate the deviation from the true value. To precisely measure the error, the signal-to-noise ratio (SNR) of the slip ratio is introduced for evaluation, which is given by

$$\text{SNR} = \frac{\sqrt{\frac{1}{t} \int_0^t e_{\text{slip}}^2(t) dt}}{\frac{1}{t} \int_0^t \lambda_c(t) dt} \quad (29)$$

3.4. Virtual Prototype Validation for the SIWMS

In this study, a virtual prototype was constructed to establish a high-fidelity multi-body model using the CATIA, ADAMS, and Matlab/Simulink environment.

The developed virtual prototype is shown in Figure 9 for demonstration. First, a complete vehicle model was developed in CATIA based on the vehicle specifications obtained from an actual IWMD EV. Then, the SIWMS model was integrated into ADAMS and the constraints of each component were established. The kinematic joints of each component were defined and the loads and drives were added. Finally, the braking torques of the caliper and IWM in ADAMS were taken from the brake controller and IWM system modules in the MatLab/Simulink, respectively. The radial UEMF was applied on the rotor and stator surfaces of IWM. The vehicle responses of the virtual prototype model and the numerical model of the SIWMS in the vertical and longitudinal directions are compared in Figure 10. The error statistics are listed in Table 3.

Table 3. The selected evaluation indexes.

Response Variables	Numerical Model	VP Model	Error
RVA/(m/s ²)	0.4353	0.4157	4.71%
RTDL/(N)	296.5	282.6	4.92%
LAFR/(m/s ²)	10.77	11.03	2.36%
SNR/(%)	31.17	32.55	4.24%

As shown in Figure 10a–d, the two models demonstrate the same trend in all response variables with marginal lag time. The main distinction between the two models lies in the longitudinal direction. In particular, the proposed SIWMS model is validated by comparing the selected evaluation indexes as shown in Table 3. It can be seen that all the errors are within 5%, which verifies the validity of the proposed model [60].

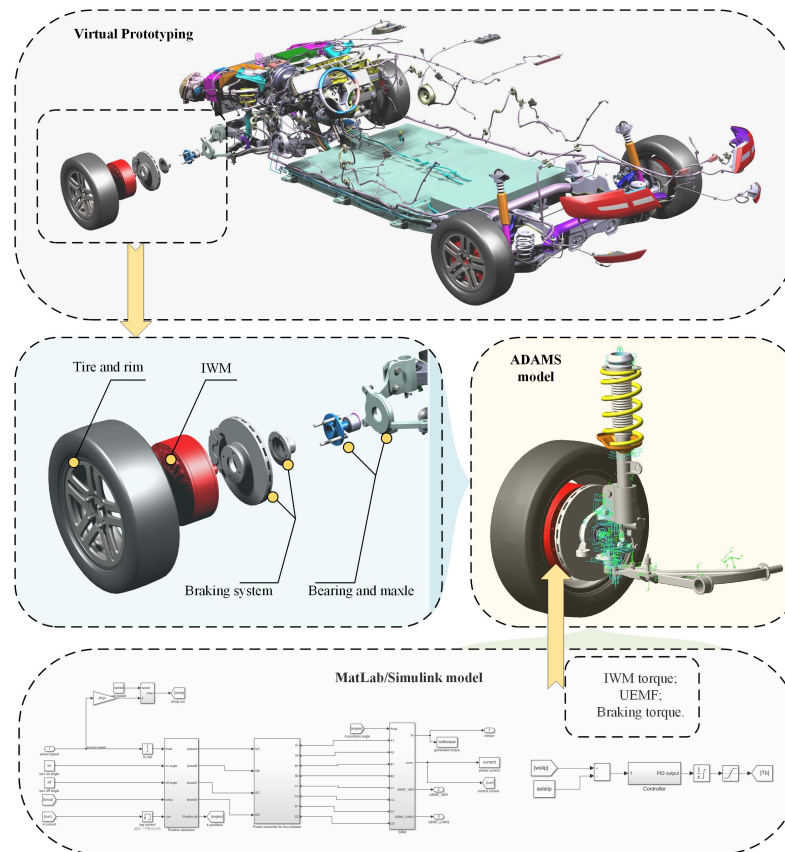


Figure 9. The build process of the VP model.

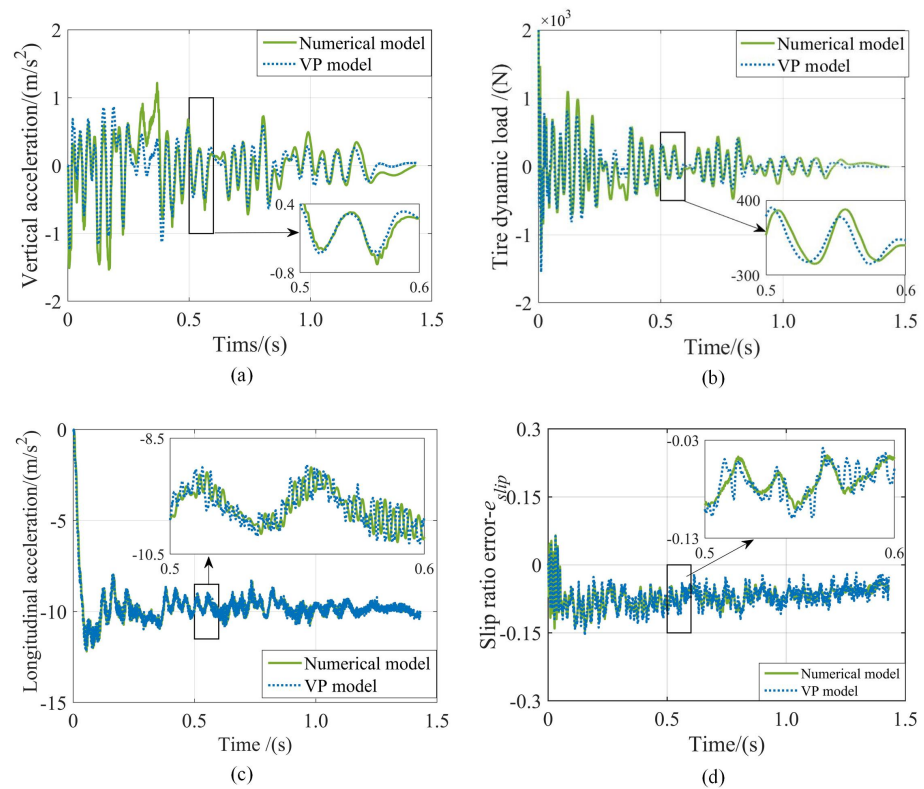


Figure 10. Simulation results obtained from the virtual prototype model and the proposed numerical model of SIWMS: (a) vertical acceleration of the vehicle; (b) dynamic load of the tire; (c) slip ratio on the dry asphalt road; (d) slip ratio error- e_{slip} .

4. UEMF Effects and SIWMS Optimization

In this section, a simulation comparison is performed with and without considering UEMF. Four key parameters are selected and their effects on vehicle vertical–longitudinal dynamics are investigated. Furthermore, the key stiffness and damping parameters are optimized using a multi-objective optimization algorithm.

4.1. Analysis of UEMF Effects

4.1.1. Relationship between UEMF and Eccentricity

Due to the resultant UEMF, the dynamic eccentricity of the IWM due to the road input and slip ratio fluctuations has a remarkable impact on vehicle dynamics. To obtain the vertical and longitudinal eccentricity values of the IWM during braking and the vertical and longitudinal UEMFs generated by the IWM, numerical analysis was performed using the model validated in the previous subsection. The results are shown in Figure 11.

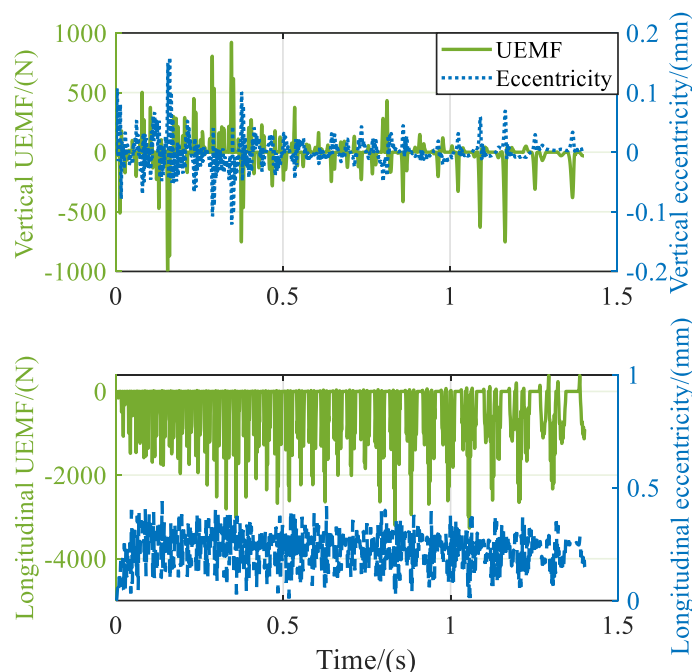


Figure 11. The UEMF and eccentricity calculation results.

It can be seen that the IWM has dynamic eccentricities and UEMFs in both the vertical and longitudinal directions. In the vertical direction, the eccentricity is random. This leads to a random state of the vertical UEMF that varies from -1000 N to 1000 N. In the longitudinal direction, the eccentricity between the stator and the rotor is always positive, as the overall acceleration is negative during the braking process. Moreover, its corresponding longitudinal UEMF is negative and varies from 0 N to 2500 N, with the same order of magnitude as in the vertical direction.

4.1.2. UEMF Effects

The UEMF has a significant effect on vehicle dynamics. Additional simulation results are shown in Table 4.

Table 4. Evaluation indexes for vehicle dynamics during braking.

	With UEFM	Without UEFM	Percentage of Degradation		With UEFM	Without UEFM	Percentage of Degradation
ISO-A and Dry asphalt				ISO-B and Dry asphalt			
RVA (m/s ²)	0.4353	0.4325	0.65	RVA (m/s ²)	0.9081	0.8935	1.63
RTDL (N)	296.5	295.3	0.41	RTDL (N)	631.2	622.2	1.45
LAFR (%)	10.77	10.66	1.03	LAFR (%)	12.82	12.27	4.48
SNR (%)	31.17	30.67	1.63	SNR (%)	36.58	34.61	5.69
ISO-A and Cobblestone				ISO-B and Cobblestone			
RVA (m/s ²)	0.4764	0.4734	0.63	RVA (m/s ²)	0.9413	0.931	1.11
RTDL (N)	321.8	320.5	0.41	RTDL (N)	700.3	687.3	1.89
LAFR (%)	6.937	6.796	2.07	LAFR (%)	10.26	9.72	5.56
SNR (%)	31.49	30.76	2.37	SNR (%)	37.22	34.79	6.98

According to the comparison results shown in Table 4, the RVA and RTDL are slightly increased when the effect of UMF is considered, while the increases in LAFR and SNR are more profound. This shows that the UEMF caused by magnet gap deformation negatively affects the ride comfort and longitudinal stability of the vehicle. During braking, UEMF has a greater effect on the longitudinal dynamics than on the vertical dynamics. Moreover, the effects on the ISO-B and cobblestone roads are more noticeable.

4.2. Sensitivity Analysis and Optimization

In this section, the influence of the IWM system parameters on vertical–longitudinal dynamics is investigated and a multi-objective optimization approach is employed to optimize the system parameters.

4.2.1. Sensitivity Analysis

To meet multiple design requirements, a comprehensive sensitivity analysis method is applied to evaluating the influence of each vehicle parameter on the selected optimized objectives including RVA, RTDL, LAFR, and SNR. According to previous investigations [31,61] and our preliminary analysis, k_{sus} , c_{sus} , k_{trt} , and k_{bear} were selected as the key parameters to be optimized. The original parameter values listed in Table 2 were taken as the benchmark and each value was set to 0.5/1/1.5/2 times the benchmark value, respectively. The numerical analysis was conducted while keeping the other parameters constant. To ensure that the response quantities of each index were comparable, normalized dimensionless processing was performed using

$$x^*(i) = \frac{x(i) - \eta}{\sigma} \quad (30)$$

where $x^*(i)$ is the converted value, $x(i)$ is the initial value, and η and σ are the mean and standard deviations of all sample data. Generally, a larger value of $x^*(i)$ indicates more significant influence on the optimization objectives, while the positive curve slope indicates that the optimization objective will increase with the increasing design variable and vice versa. Thus, the sensitivity of each selected design parameter on the optimization objectives can be calculated. The results are shown in Figure 12.

As seen from Figure 12, each parameter exhibits different levels of sensitivity to the optimization objectives. Specifically, the RVA and LAFR demonstrate similar increasing trends, with k_{sus} increasing from 0.5 up to twice the initial value. For c_{sus} and k_{bear} , the RTDL and SNR reflect a constant trend of sensitivity, with c_{sus} being negative and k_{bear} being positive. However, the evaluation indexes with the same trend for k_{trt} are LAFR and SNR.

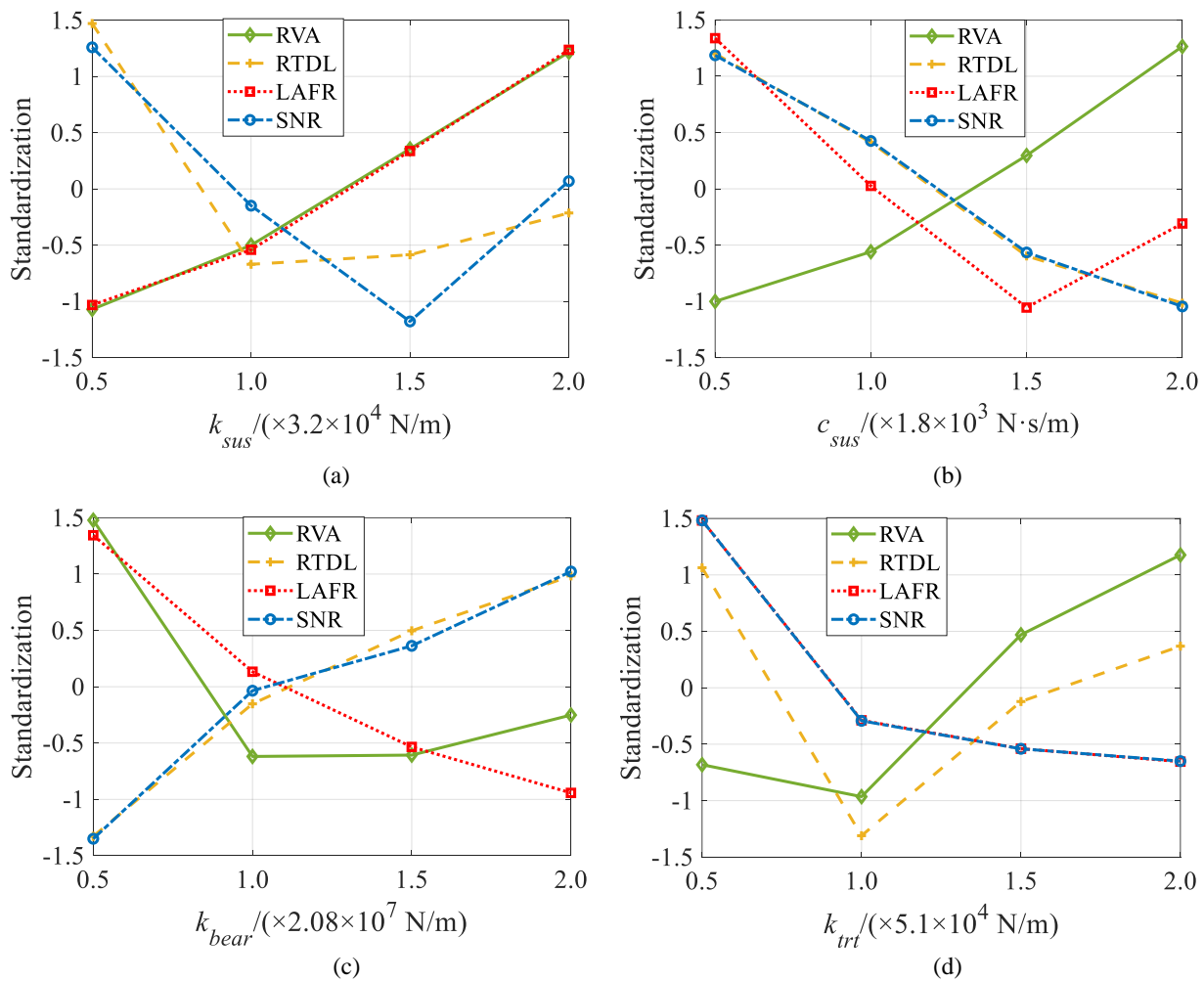


Figure 12. The influence of the IWM system parameters on dynamics evaluation indexes: (a) k_{sus} ; (b) c_{sus} ; (c) k_{bear} ; (d) k_{trt} .

It can be observed that key parameters have a strong sensitivity to the vertical–longitudinal dynamics of IWMD EVs. Moreover, typical vertical parameters influence the longitudinal vehicle dynamics, while longitudinal parameters affect the vertical vehicle dynamics. However, the impact is not consistent, and is sometimes even contradictory. It is relatively difficult to determine appropriate parameter values based on the sensitivity results. To improve the results, the characteristics used for these dynamics should be selected while taking the target requirements into consideration.

4.2.2. Multi-Objective Optimization of Key Parameters

To effectively solve the problem mentioned in the previous section, a technique for order preference by similarity to ideal solution (TOPSIS) is adopted to quantitatively investigate the sensitivity of each design parameter [62]. First, the decision matrix is defined as

$$D = \begin{bmatrix} x_{11} & x_{12} & \dots & x_{1n} \\ x_{21} & x_{22} & \dots & x_{2n} \\ \vdots & \vdots & \vdots & \vdots \\ x_{m1} & x_{m2} & \dots & x_{mn} \end{bmatrix} \tag{31}$$

where x_{ij} is the value for each criterion. Next, the decision matrix is normalized using

$$r_{ij} = \frac{x_{ij}}{\sqrt{\sum_{i=1}^m x_{ij}^2}} \quad (32)$$

In order to establish a normal compatible matrix, the weights of each criterion are multiplied in a normalized matrix provided by

$$v_{ij} = r_{ij} \times w_j \quad (33)$$

where w_j is the weighting factor symmetric to the j th criterion. The weighting factor can be expressed as

$$\sum_{j=1}^n w_j = 1 \quad (34)$$

The positive and negative desired values are derived as

$$\begin{aligned} A^+ &= \left\{ \left(\max_i v_{ij} \mid j \in \Omega_b \right), \left(\min_i v_{ij} \mid j \in \Omega_c \right) \right\} \\ &= \{v_j^+ \mid j = 1, 2, \dots, n\} \\ A^- &= \left\{ \left(\min_i v_{ij} \mid j \in \Omega_b \right), \left(\max_i v_{ij} \mid j \in \Omega_c \right) \right\} \\ &= \{v_j^- \mid j = 1, 2, \dots, n\} \end{aligned} \quad (35)$$

where Ω_b is related to the positive indicators and Ω_c is related to the negative ones.

The Euclidean distances from the positive and negative desired values are calculated using

$$\begin{cases} d_i^+ = \sqrt{\sum_{j=1}^n (v_{ij} - v_j^+)^2} \\ d_i^- = \sqrt{\sum_{j=1}^n (v_{ij} - v_j^-)^2} \end{cases} \quad (36)$$

Here, the relative proximity of each option, defined in terms of the closeness value Cl , is considered as the desired solution, which is provided by

$$Cl_i^* = \frac{d_i^-}{d_i^- + d_i^+} \quad (37)$$

During the braking process, longitudinal vehicle dynamics control is considered. The effects of UEMF on RVA and RTDL are not apparent. The weighting coefficient $w_1 = 0.15$ is taken for RVA while $w_2 = 0.15$ for RTDL, $w_3 = 0.3$ for LAFR and $w_4 = 0.4$ for SNR.

Each initial value is provided in Table 2, and the variation range is 0.5–2 times the initial value. The optimal values obtained by the optimization are $k_{sus} = 2.61 \times 10^4$ N/m, $c_{sus} = 2.65 \times 10^3$ N·s/m, $k_{bear} = 2.87 \times 10^7$ N/m, and $k_{trt} = 7.32 \times 10^4$ N/m. The optimization results of vehicle dynamics characteristics are shown in Figure 13a–d, while the variations of the evaluation indexes are shown in Table 5.

Table 5. Optimization results of evaluation indexes.

	RVA (m/s ²)	RTDL (N)	LAFR (%)	SNR (%)
Before optimization	0.9423	700.3	10.26	37.22
After optimization	0.9147	674.6	9.74	34.94
Optimization results	2.93% ↓	3.67% ↓	5.07% ↓	6.13% ↓

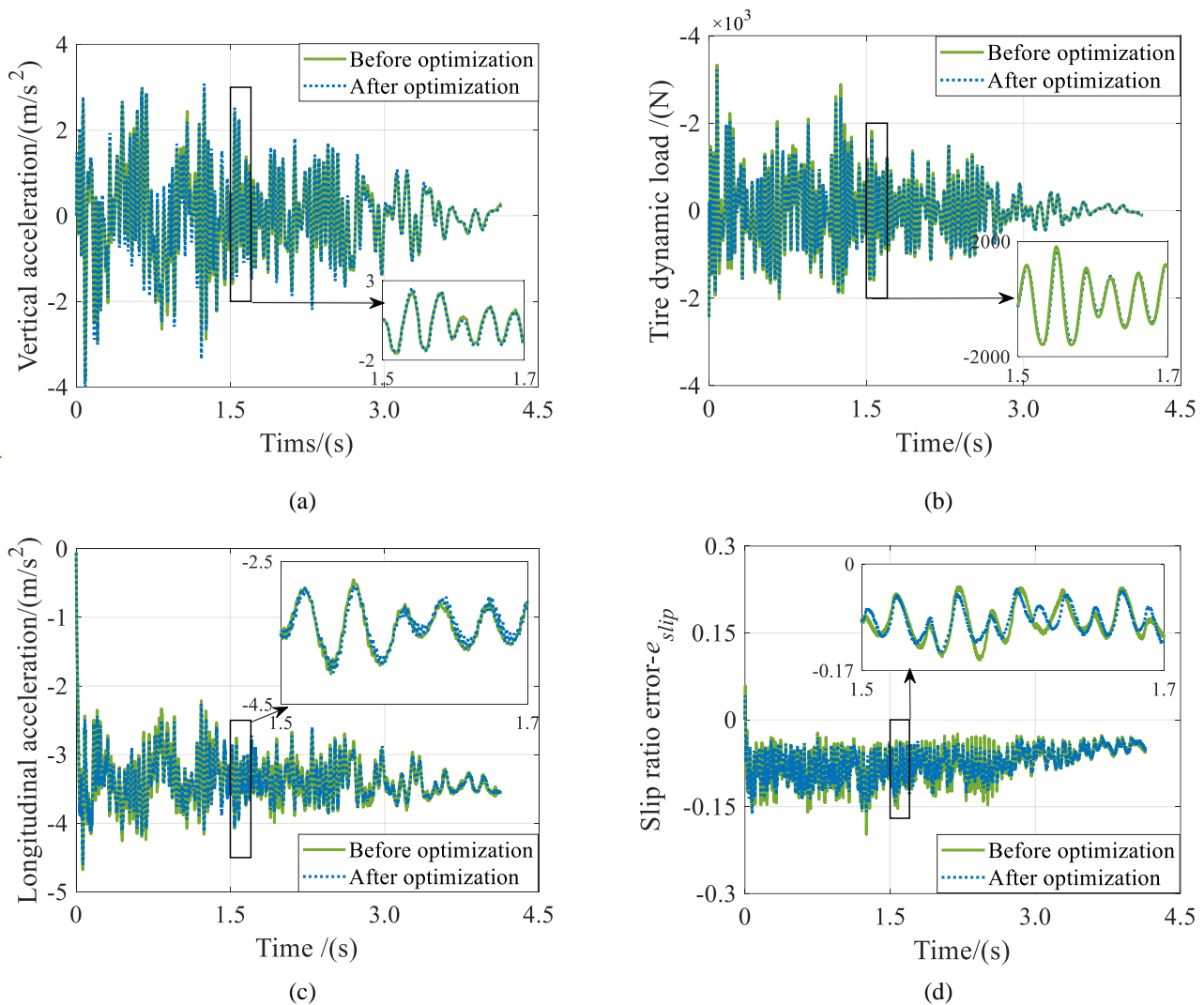


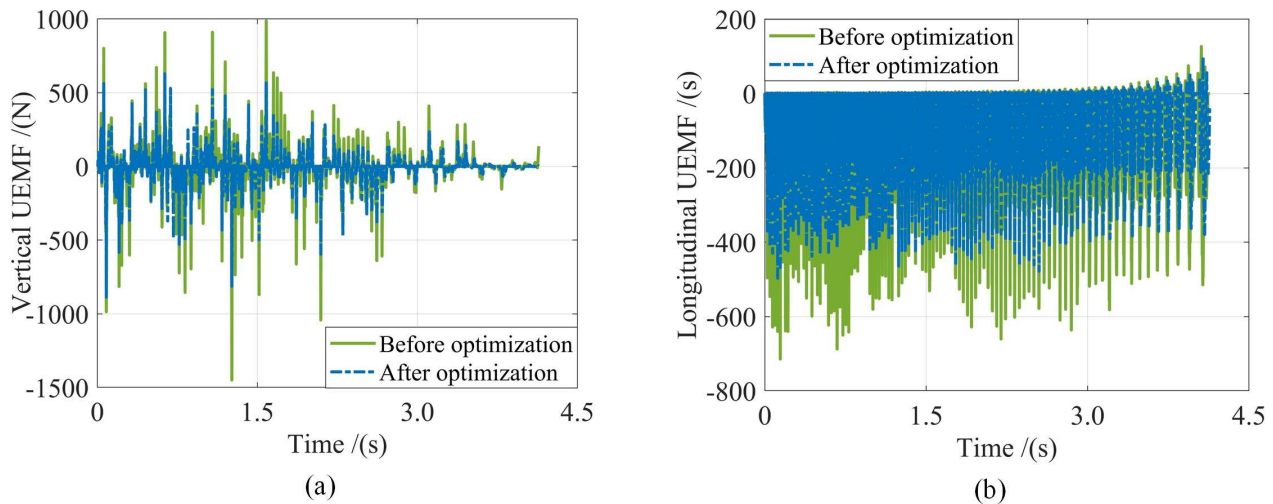
Figure 13. Optimization results of vehicle dynamics characteristics: (a) vertical acceleration of the vehicle; (b) dynamic load of the tire; (c) longitudinal acceleration of the vehicle; (d) slip ratio error e_{slip} .

All four evaluation indexes vary from 2.93% to 6.18% and are reduced after optimization. Particularly, the SNR and LAFR are reduced by 6.13% and 5.07%, respectively. The optimization results indicate that the vertical and longitudinal dynamics are improved after the proposed TOPSIS optimization and that the UEMF effects are compensated for to a certain extent. In addition, according to Figure 13, the fluctuations of vertical acceleration, dynamic load of tire, longitudinal acceleration, and slip ratio error are all suppressed. Moreover, the vertical dynamics is less affected than the longitudinal dynamics. It is worth noting that the SNR is decreased by 6.13% despite of the RMS of the slip ratio error being 0.0786 (nearly half the optimal slip ratio of 0.14), as seen in Figure 13d. The limited adjustment ranges for the tire and the bearing stiffness hinder further improvements of vehicle dynamics through parameter optimization.

The UEMF generated by the multi-field coupling effect exacerbates motor vibration, shortening the service life of motor and reducing the ride comfort of vehicle. Simulation results for UEMF are provided in Table 6, while the response comparisons are depicted in Figure 14.

Table 6. Optimization results of UEMF.

RMS	Vertical UEMF (N)	Longitudinal UEMF (N)
Before optimization	117.95	171.01
After optimization	77.02	133.06
Optimization results	34.7% ↓	22.2% ↓

**Figure 14.** Optimization results of UEMF: (a) vertical UEMF and (b) longitudinal UEMF.

Generally, multi-objective optimization can improve the vertical–longitudinal dynamic performance of a vehicle to a certain extent. In addition, it is worth noting that the influence of UEMF can be effectively reduced by the TOPSIS algorithm.

5. Conclusions

In this paper, a complete and thorough investigation on the vertical–longitudinal coupling effects of in-wheel-motor-drive electric vehicles (IWMD EVs) is conducted. A comprehensive suspension-in-wheel-motor system (SIWMS) model is first established, in which a road–tire–ring force (RTRF) model is built to simultaneously capture the vertical and longitudinal vehicle dynamics. Further investigations are then conducted under different braking maneuvers with various road conditions to reveal the negative effects of road–tire–ring force (UEMF) on vehicle dynamics. Furthermore, a virtual prototype environment is developed to validate the efficacy of the developed SIWMS. Four key parameters are optimized using a multi-objective optimization method. The simulation results show that UEMF can significantly compromise longitudinal vehicle dynamics while slightly affecting vertical dynamics. Through optimization, the longitudinal acceleration rate and the signal-to-noise ratio of the slip ratio are respectively reduced by 5.07% and 6.13%, while the UEMF in the vertical and longitudinal directions are reduced to the ranges of from 22.2% to 34.7%, indicating improved the ride comfort and handling performance of vehicle.

Author Contributions: Data curation, Z.Z. and L.G.; Methodology, J.W. and S.L.; Project administration, J.W. and L.G.; Resources, L.Z. and J.W.; Software, S.L.; Supervision, L.Z. and L.G.; Validation, L.Z.; Visualization, Z.Z.; Writing—original draft, Z.Z. and L.Z.; Writing—review and editing, Z.Z. and L.Z. All authors have read and agreed to the published version of the manuscript.

Funding: This research was supported in part by the National Natural Science Foundation of China (Grant No. 52272387 and Grant No. 52202457) and in part by the State Key Laboratory of Mechanical Behavior and System Safety of Traffic Engineering Structures, Shijiazhuang Tiedao University (Grant KF2020-29).

Institutional Review Board Statement: Not applicable.

Informed Consent Statement: The data involved in this paper do not involve ethical issues.

Data Availability Statement: The datasets used and analyzed during the current study are available from the corresponding author on reasonable request.

Conflicts of Interest: All authors certify that they have no affiliations with or involvement in any organization or entity with any financial interest or non-financial interest in the subject matter or materials discussed in this manuscript.

References

1. Zhao, Z.; Taghavifar, H.; Du, H.; Qin, Y.; Dong, M.; Gu, L. In-wheel motor vibration control for distributed-driven electric vehicles: A review. *IEEE Trans. Transp. Electrification*. **2021**, *7*, 2864–2880. [[CrossRef](#)]
2. Zhang, L.; Zhang, Z.; Wang, Z.; Deng, J.; Dorrell, D. Chassis coordinated control for full X-by-wire vehicles—A review. *Chin. J. Mech. Eng.* **2021**, *34*, 1–25. [[CrossRef](#)]
3. He, S.; Fan, X.; Wang, Q.; Chen, X.; Zhu, S. Review on Torque Distribution Scheme of Four-Wheel In-Wheel Motor Electric Vehicle. *Machines* **2022**, *10*, 619. [[CrossRef](#)]
4. Bilgin, B.; Liang, J.; Terzic, M.V.; Dong, J.; Rodriguez, R.; Trickett, E.; Emadi, A. Modeling and analysis of electric motors: State-of-the-art review. *IEEE Trans. Transp. Electrification*. **2019**, *5*, 602–617. [[CrossRef](#)]
5. Wu, J.; Wang, Z.; Zhang, L. Unbiased-estimation-based and computation-efficient adaptive MPC for four-wheel-independently-actuated electric vehicles. *Mech. Mach. Theory* **2020**, *154*, 104100. [[CrossRef](#)]
6. Dukalski, P.; Będkowski, B.; Parczewski, K.; Wnęk, H.; Urbaś, A.; Augustynek, K. Dynamics of the vehicle rear suspension system with electric motors mounted in wheels. *Ekspluat. i Niezawodn.* **2019**, *21*, 125–136. [[CrossRef](#)]
7. Zhang, C.; Zhang, X.; Zhao, F.; Gerada, D.; Li, L. Improvements on Permanent Magnet Synchronous Motor by Integrating Heat Pipes Into Windings for Solar Unmanned Aerial Vehicle. *Green Energy Intell. Transp.*, **2022**, *1*, 100011. [[CrossRef](#)]
8. Islam, R.; Husain, I. Analytical model for predicting noise and vibration in permanent-magnet synchronous motors. *IEEE Trans. Ind. Appl.* **2010**, *46*, 2346–2354. [[CrossRef](#)]
9. Smith, A.; Dorrell, D. Calculation and measurement of unbalanced magnetic pull in cage induction motors with eccentric rotors. Part 1: Analytical model. *IEE Proc.-Electr. Power Appl.* **1996**, *143*, 193–201. [[CrossRef](#)]
10. Dukalski, P.; Będkowski, B.; Parczewski, K.; Wnęk, H.; Urbaś, A.; Augustynek, K. Analysis of the influence of motors installed in passenger car wheels on the torsion beam of the rear axle suspension. *Energies* **2022**, *15*, 222. [[CrossRef](#)]
11. Carmeli, M.S.; Dezza, F.C.; Mauri, M. Electromagnetic vibration and noise analysis of an external rotor permanent magnet motor. In Proceedings of the International Symposium on Power Electronics, Electrical Drives, Automation and Motion, Taormina, Italy, 23–26 May 2006; pp. 1028–1033.
12. Wang, Y.y.; Yang, F.n. SRM representative parameters effect on in-wheel motored vehicle performance. In Proceedings of the 2017 2nd IEEE International Conference on Intelligent Transportation Engineering (ICITE), Singapore, 1–3 September 2017, pp. 36–41.
13. Li, J.; Cho, Y. Dynamic reduction of unbalanced magnetic force and vibration in switched reluctance motor by the parallel paths in windings. *Math. Comput. Simul.* **2010**, *81*, 407–419. [[CrossRef](#)]
14. Qin, Y.; He, C.; Shao, X.; Du, H.; Xiang, C.; Dong, M. Vibration mitigation for in-wheel switched reluctance motor driven electric vehicle with dynamic vibration absorbing structures. *J. Sound Vib.* **2018**, *419*, 249–267. [[CrossRef](#)]
15. Xu, B.; Xiang, C.; Qin, Y.; Ding, P.; Dong, M. Semi-active vibration control for in-wheel switched reluctance motor driven electric vehicle with dynamic vibration absorbing structures: Concept and validation. *IEEE Access* **2018**, *6*, 60274–60285. [[CrossRef](#)]
16. Qin, Y.; Wang, Z.; Yuan, K.; Zhang, Y. Comprehensive analysis and optimization of dynamic vibration-absorbing structures for electric vehicles driven by in-wheel motors. *Automot. Innov.* **2019**, *2*, 254–262. [[CrossRef](#)]
17. Shieh, M.Y.; Chiou, J.S.; Liu, M.T. Design of immune-algorithm-based adaptive fuzzy controllers for active suspension systems. *Adv. Mech. Eng.* **2014**, *6*, 916257. [[CrossRef](#)]
18. Sunwoo, M.; Cheok, K.C.; Huang, N. Model reference adaptive control for vehicle active suspension systems. *IEEE Trans. Ind. Electron.* **1991**, *38*, 217–222. [[CrossRef](#)]
19. Chen, S.A.; Wang, J.C.; Yao, M.; Kim, Y.B. Improved optimal sliding mode control for a non-linear vehicle active suspension system. *J. Sound Vib.* **2017**, *395*, 1–25. [[CrossRef](#)]
20. Badri, P.; Amini, A.; Sojoodi, M. Robust fixed-order dynamic output feedback controller design for nonlinear uncertain suspension system. *Mech. Syst. Signal Process.* **2016**, *80*, 137–151. [[CrossRef](#)]
21. Zhu, J.; Wang, Z.; Zhang, L.; Dorrell, D.G. Braking/steering coordination control for in-wheel motor drive electric vehicles based on nonlinear model predictive control. *Mech. Mach. Theory* **2019**, *142*, 103586. [[CrossRef](#)]
22. Mao, Y.; Zuo, S.; Wu, X.; Duan, X. High frequency vibration characteristics of electric wheel system under in-wheel motor torque ripple. *J. Sound Vib.* **2017**, *400*, 442–456. [[CrossRef](#)]
23. Li, T.; Zhang, S.; Xiao, G.; Wang, M.; Zhong, H.; Feng, J. Brake Instability Dynamic Model and Active Control Strategy for a Multiunit Articulated Rubber-Wheel Autonomous Rail Rapid Transit System. *Sustainability* **2022**, *14*, 14531. [[CrossRef](#)]
24. Kambe, H.; Koumura, S. Reduction of longitudinal vibration by side-view arrangement of suspension. *Veh. Syst. Dyn.* **2008**, *46*, 161–173. [[CrossRef](#)]
25. Zuo, S.; Duan, X.; Wu, X. Modeling and analysis of rigid ring coupling model of electric wheel. *Nat. Sci.* **2014**, *42*, 1578–1585.

26. Wang, Z.; Wang, Y.; Zhang, L.; Liu, M. Vehicle stability enhancement through hierarchical control for a four-wheel-independently-actuated electric vehicle. *Energies* **2017**, *10*, 947. [[CrossRef](#)]
27. Zhao, W.; Qin, X. Study on mixed H_2/H_∞ robust control strategy of four wheel steering system. *Sci. China Technol. Sci.* **2017**, *60*, 1831–1840. [[CrossRef](#)]
28. Wu, J.; Cheng, S.; Liu, B.; Liu, C. A human-machine-cooperative-driving controller based on AFS and DYC for vehicle dynamic stability. *Energies* **2017**, *10*, 1737. [[CrossRef](#)]
29. Zhang, J.; Yang, Y.; Hu, M.; Yang, Z.; Fu, C. Longitudinal–vertical comprehensive control for four-wheel drive pure electric vehicle considering energy recovery and ride comfort. *Energy* **2021**, *236*, 121417. [[CrossRef](#)]
30. Song, L.; Li, J.; Wei, Z.; Yang, K.; Hashemi, E.; Wang, H. Longitudinal and Lateral Control Methods from Single Vehicle to Autonomous Platoon. *Green Energy Intell. Transp.* **2023**, 100066. [[CrossRef](#)]
31. Qin, Y.; Zhao, Z.; Wang, Z.; Li, G. Study of longitudinal–vertical dynamics for in-wheel motor-driven electric vehicles. *Automot. Innov.* **2021**, *4*, 227–237. [[CrossRef](#)]
32. Xing, C.; Zhu, Y.; Wu, H. Electromechanical Coupling Braking Control Strategy Considering Vertical Vibration Suppression for Vehicles Driven by In-Wheel Motors. *IEEE/ASME Trans. Mechatronics* **2022**, *27*, 5701–5711. [[CrossRef](#)]
33. Ricciardi, V.; Ivanov, V.; Dhaens, M.; Vandersmissen, B.; Geraerts, M.; Savitski, D.; Augsburg, K. Ride blending control for electric vehicles. *World Electr. Veh. J.* **2019**, *10*, 36. [[CrossRef](#)]
34. Li, Z.; Zheng, L.; Gao, W.; Zhan, Z. Electromechanical coupling mechanism and control strategy for in-wheel-motor-driven electric vehicles. *IEEE Trans. Ind. Electron.* **2018**, *66*, 4524–4533. [[CrossRef](#)]
35. Deur, J.; Asgari, J.; Hrovat, D. A 3D brush-type dynamic tire friction model. *Veh. Syst. Dyn.* **2004**, *42*, 133–173. [[CrossRef](#)]
36. Besselink, I.; Schmeitz, A.; Pacejka, H. An improved Magic Formula/Swift tyre model that can handle inflation pressure changes. *Veh. Syst. Dyn.* **2010**, *48*, 337–352. [[CrossRef](#)]
37. Zegelaar, P.; Pacejka, H. Dynamic tyre responses to brake torque variations. *Veh. Syst. Dyn.* **1997**, *27*, 65–79. [[CrossRef](#)]
38. Gipser, M. FTire: A physically based application-oriented tyre model for use with detailed MBS and finite-element suspension models. *Veh. Syst. Dyn.* **2005**, *43*, 76–91. [[CrossRef](#)]
39. Xue, X.; Cheng, K.W.E.; Lin, J.; Zhang, Z.; Luk, K.; Ng, T.W.; Cheung, N.C. Optimal control method of motoring operation for SRM drives in electric vehicles. *IEEE Trans. Veh. Technol.* **2010**, *59*, 1191–1204. [[CrossRef](#)]
40. Anwar, M.; Husain, I. Radial force calculation and acoustic noise prediction in switched reluctance machines. *IEEE Trans. Ind. Appl.* **2000**, *36*, 1589–1597. [[CrossRef](#)]
41. Jokinen, T.; Hrabovcova, V.; Pyrhonen, J. *Design of Rotating Electrical Machines*; John Wiley & Sons: Hoboken, NJ, USA, 2013.
42. Zhu, W.; Pekarek, S.; Fahimi, B.; Deken, B.J. Investigation of force generation in a permanent magnet synchronous machine. *IEEE Trans. Energy Convers.* **2007**, *22*, 557–565. [[CrossRef](#)]
43. Ito, T.; Akatsu, K. Electromagnetic force acquisition distributed in electric motor to reduce vibration. *IEEE Trans. Ind. Appl.* **2016**, *53*, 1001–1008. [[CrossRef](#)]
44. Krishnan, R. *Switched Reluctance Motor Drives: Modeling, Simulation, Analysis, Design, and Applications*; CRC Press: Boca Raton, FL, USA, 2017.
45. Ebrahimi, B.M.; Faiz, J.; Roshtkhari, M.J. Static-, dynamic-, and mixed-eccentricity fault diagnoses in permanent-magnet synchronous motors. *IEEE Trans. Ind. Electron.* **2009**, *56*, 4727–4739. [[CrossRef](#)]
46. Qin, Y.; Wang, Z.; Xiang, C.; Hashemi, E.; Khajepour, A.; Huang, Y. Speed independent road classification strategy based on vehicle response: Theory and experimental validation. *Mech. Syst. Signal Process.* **2019**, *117*, 653–666. [[CrossRef](#)]
47. Qin, Y.; Wei, C.; Tang, X.; Zhang, N.; Dong, M.; Hu, C. A novel nonlinear road profile classification approach for controllable suspension system: Simulation and experimental validation. *Mech. Syst. Signal Process.* **2019**, *125*, 79–98. [[CrossRef](#)]
48. Rajamani, R. *Vehicle Dynamics and Control*; Springer Science & Business Media: Berlin/Heidelberg, Germany, 2011.
49. Soares, C.M.; Martins, J.; Rodrigues, H.; Ambrosio, J.A.; Pina, C.; Soares, C.M.; Pereira, E.; Folgado, J. *III European Conference on Computational Mechanics: Solids, Structures and Coupled Problems in Engineering: Book of Abstracts*; Springer Science & Business Media: Berlin/Heidelberg, Germany, 2008.
50. Canudas-de Wit, C.; Tsiotras, P.; Velenis, E.; Basset, M.; Gissinger, G. Dynamic friction models for road/tire longitudinal interaction. *Veh. Syst. Dyn.* **2003**, *39*, 189–226. [[CrossRef](#)]
51. Ding, X.; Wang, Z.; Zhang, L.; Liu, J. A Comprehensive vehicle stability assessment system based on enabling tire force estimation. *IEEE Trans. Veh. Technol.* **2022**, *71*, 11571–11588. [[CrossRef](#)]
52. Kindt, P.; Sas, P.; Desmet, W. Measurement and analysis of rolling tire vibrations. *Opt. Lasers Eng.* **2009**, *47*, 443–453. [[CrossRef](#)]
53. Wang, H.; Al-Qadi, I.L.; Stanciulescu, I. Simulation of tyre–pavement interaction for predicting contact stresses at static and various rolling conditions. *Int. J. Pavement Eng.* **2012**, *13*, 310–321. [[CrossRef](#)]
54. Mousseau, C.; Laursen, T.; Lidberg, M.; Taylor, R. Vehicle dynamics simulations with coupled multibody and finite element models. *Finite Elem. Anal. Des.* **1999**, *31*, 295–315. [[CrossRef](#)]
55. Maurice, J.; Berzeri, M.; Pacejka, H. Pragmatic tyre model for short wavelength side slip variations. *Veh. Syst. Dyn.* **1999**, *31*, 65–94. [[CrossRef](#)]
56. Ozerem, O.; Morrey, D. A brush-based thermo-physical tyre model and its effectiveness in handling simulation of a Formula SAE vehicle. *Proc. Inst. Mech. Eng. Part J. Automob. Eng.* **2019**, *233*, 107–120. [[CrossRef](#)]

57. Guo, Z.; Wu, W.; Yuan, S. Longitudinal-vertical dynamics of wheeled vehicle under off-road conditions. *Veh. Syst. Dyn.* **2022**, *60*, 470–490. [[CrossRef](#)]
58. Tuononen, A.; Hartikainen, L.; Petry, F.; Westermann, S. Parameterization of in-plane rigid ring tire model from instrumented vehicle measurements. In Proceedings of the 11th International Symposium on Advanced Vehicle Control (AVEC'12), Seoul, Republic of Korea, 9–12 September 2012; pp. 9–12.
59. Albers, A.; Zingel, C.; Zehetner, J.; Meitz, K. *Influence of Low-Frequency Powertrain-Vibrations on Driveability-Assessments*; Technical Report, SAE Technical Paper; SAE: Warrendale, PA, USA, 2010.
60. Guiggiani, M. *The Science of Vehicle Dynamics*; Springer: Pisa, Italy; Cham, The Netherlands, 2014; p. 15.
61. Song, Z.; Li, J.; Wei, Y.; Xu, L.; Ouyang, M. Interaction of in-wheel permanent magnet synchronous motor with tire dynamics. *Chin. J. Mech. Eng.* **2015**, *28*, 470–478. [[CrossRef](#)]
62. Jiang, R.; Wang, D. *Optimization of Vehicle Ride Comfort and Handling Stability Based on TOPSIS Method*; Technical report; SAE Technical Paper; SAE: Warrendale, PA, USA, 2015.

Disclaimer/Publisher's Note: The statements, opinions and data contained in all publications are solely those of the individual author(s) and contributor(s) and not of MDPI and/or the editor(s). MDPI and/or the editor(s) disclaim responsibility for any injury to people or property resulting from any ideas, methods, instructions or products referred to in the content.